

Mechanical Evaluation of WC-Co Materials with Varying Microstructures

John J. Pittari III^{}, Jeffrey J. Swab, Jared Wright[†], and Katherine Atwater[‡]*

ABSTRACT

Tungsten carbide-cobalt materials are useful in a variety of extreme applications due to a desirable blend of properties, yet the technology has not significantly changed since their initial development in the 1920s. The mechanical properties of this class of materials is highly dependent on two variables, the size of the tungsten carbide grains, and the amount of binder phase present in the final body. In this study, the amount of binder phase is isolated across three commercial materials from the same manufacturer with three different grain sizes to investigate the effect on mechanical properties. The mechanical properties investigated are indentation hardness, flexure and tensile strength, as well as fracture toughness. In general, an increase in hardness and tensile strength with decreasing grain size was observed, while the fracture toughness showed the opposite trend with toughness increasing with increasing grain size. The flexure strength results did not show a correlation to grain size. Fractographic analysis identified the dominant strength-limiting flaw for each sample, which largely were in the form of porosity. Other flaws types, such as inclusions from the milling process, clusters of large grains, and machining cracks from the surface finishing process, were also identified. Weibull analysis was performed and deemed appropriate for analysis of these materials, but strength-size scaling was not conducted due to the variability in the strength-limiting feature between the different specimen geometries.

Keywords: Tungsten Carbide, Uniaxial Tensile Strength, Flexure Strength, Fracture Toughness, Fractography, Weibull Analysis

1.0 BACKGROUND

Cemented carbide materials are implemented in a wide array of applications where their unique blend of properties results in improved performance. Typically, the application space for these materials is under extreme temperature and pressure environments, such as the conditions seen during machining, grinding, and bearing. The majority of their applications reside in the machining industry, as tools for geologic mining and drilling, turning of specialty metals [1-3], wear parts and coatings [2], and bulk components. These materials possess a rare

^{*} Now with The Boeing Company, Jacksonville, FL

[†] Now with NAVAIR – Patuxent River, MD

[‡] Now with Northrop Grumman, Grafton, MA

combination of excellent hardness and toughness, which are typically inversely related [4-7]. The most common cemented carbide is composed of hard tungsten carbide (WC) grains cemented in a ductile cobalt binder matrix phase, sometimes simply referred to as “carbide”. Tungsten carbide itself has an elastic modulus over twice that of steel [8-10] and a Vickers hardness (HV) of 1800-2000 kgf/mm² [8], comparable to other ultra-hard ceramics, such as alumina and silicon carbide. Cobalt (Co) has historically been used in the aerospace industry in super alloys due to its exceptional temperature, corrosion, and wear resistance [8, 11-15]. The marrying of these two wildly different phases into one body is what imparts the exceptional performance of these parts in various applications.

The technology of cemented carbides has seen gradual improvement over the last century of use [2, 16, 17]. The quality of raw materials has increased, and innovative processing techniques have reduced the size of strength-limiting flaws [18, 19], bringing substantial improvements in mechanical performance. The properties and performance of carbide parts are typically dictated by the carbide grain size/distribution, the binder phase composition/content, and any additive phases. Both the carbide grain size and binder content have an influence on the hardness-toughness trade-off, as increasing binder content typically increases the toughness through the increased presence of the ductile cobalt phase, while decreasing the grain size increases the hardness [20-27], per a typical Hall-Petch relationship [28, 29], yet reduces the toughness by decreasing the tortuosity of the crack plane. Understanding how to properly balance both of these elements in selecting a component with a desired performance is critical towards reaping the full benefit of their unique blend of properties. Many investigations have examined alternate binder materials to achieve better property control, but no overarching outcomes have been identified [1, 4, 30-36]. On the other hand, compounds can be purposefully added into the WC-Co powder mixture, which affect the resultant properties. Improvements have been realized with the inclusion of additives into the binder phase to inhibit grain growth and dislocation motion [1, 15, 36-40]. These modifications influence the final microstructure of the material, which is useful in tailoring the hardness and toughness properties. Typically, carbides such as titanium carbide (TiC), tantalum carbide (TaC), and vanadium carbide (VC), amongst numerous others, are included to act as grain refining phases to prevent exaggerated growth of the WC grains during sintering [15, 16, 37, 41-44]. Chromium and nickel, or compounds containing these elements, such as chromium carbide (Cr₃C₂) or nichrome (NiCr), can be added to improve the oxidation resistance of the final part [2, 16, 41, 45].

The purpose of the current investigation was to evaluate the material properties of a suite of commercially-available tungsten carbide-cobalt materials that possess similar cobalt binder content but variations in microstructure, resulting in corresponding differences in properties. Apart from the manufacturer documentation and limited technical literature, there is very little known about the properties of these **four** materials. This paper summarizes the characterization and mechanical testing of four materials.

2.0 MATERIALS

The objective of this study was to understand how differences in WC grain size affected the mechanical properties of tungsten carbide-cobalt composites. Materials with comparable cobalt content, but differing microstructures, were sought for evaluation against another commercially-available tungsten carbide-cobalt that has been previously investigated [46]. The comparison material is the Kennametal S105 (Latrobe, PA), now known as KFS64. Three commercially-available tungsten carbide-cobalt materials, manufactured by the Ceratizit Group (Mamer, Luxembourg), were examined in this study. The three materials investigated had essentially the same cobalt content, but significantly different tungsten carbide grain sizes. The manufacturer-supplied information on all four materials is presented in Table 1.

Table 1. Manufacturer-supplied information on WC-Co materials being evaluated.

Vendor	Vendor Code	Co Binder [wt.%]	Density [g/cc]	Nominal Grain Size [μm]	Vickers Hardness, HV30 [N/mm^2]
Ceratizit	CTF24F (Fine)	12.0	14.32	1.85	1340
Ceratizit	CTS23H (Submicron)	11.5*	14.25	0.8	1630
Ceratizit	TSF44h5 (Ultrafine)	12.0^	14.10	0.4	1730
Kennametal	S105†	10.0‡	14.40	0.5-0.8	1580

*Additionally includes <0.5% VC and <0.5% Cr_3C_2

^Additionally includes <0.5% VC and 1.0% Cr_3C_2

†Now labeled as KFS64

‡Additionally includes 0.6% Cr

Due to a supply issue, the TSF44h5 (Ultrafine) material had to be acquired from the Ceratizit domestic supplier[§]. As a result, the rods had different final surface finishes. To the naked eye,

[§] Ceratizit Michigan Inc., 11350 Stephens Drive, Warren, MI 48089

the CTF24F and CTS23H have very similar finishes, while the TSF44h5 had a very shiny surface compared to the other three. S105 had the dullest surface finish of the four materials.

All three Ceratizit carbide materials were obtained in two forms of rod stock: (1) nominally 16 mm in diameter and 330 mm in length, and (2) nominally six mm diameter rods of varying lengths. (The TSF44h5 (Ultrafine) rods had a length of nominally 330 mm while the rods of CTF24F (Fine) and CTS23H (Submicron) had a length of nominally 50 mm.) In all cases the rods had a circumferentially ground surface finish on the diameter. The larger diameter rods were used to machine uniaxial tensile specimens, per the drawing in Figure 1, while the smaller diameter rods were used for cylindrical flexure strength, and some were machined into rectangular beams for fracture toughness testing.

3.0 EXPERIMENTAL PROCEDURE

3.1 Density, Elastic Properties & Microstructures

The density of each rod was determined according to the Archimedes method. Elastic properties were obtained from resonant ultrasound spectroscopy (RUS) scans of each part. Microstructural characterization was completed by examining polished sections of each material using a scanning electron microscope (SEM).

3.2 Mechanical Properties

Knoop indentation hardness values were obtained at a load of 2000 gf (19.6 N) for each material, following the procedures in ASTM C1326 [47]**. The four-point flexure strength of the 6-mm-diameter rods was determined following the testing procedures in ASTM C1684 [48]. Thirty rod specimens were tested for each of the Ceratizit materials while twenty rods were tested for the S105. Tensile test specimens were machined from the 16-mm-diameter rods, as per the drawing in Figure 1, by an outside contractor, and these specimens were used to determine the uniaxial tensile strength of each material, according to ASTM C1273 [49]. Approximately fifteen tensile specimens were tested for each material. Prismatic beam specimens, nominally 3 x 4 x 50 mm³ in size, were machined from several of the 6-mm-diameter rods, according to the guidelines in ASTM C1421 [50], so that the single-edge, precracked beam (SEPB) method could be used to determine the fracture toughness. **The SEPB precrack can be generated by placing an indent, a series of aligned indents, or a notch into the**

**Vickers hardness is the typical hardness value reported for hard metals while Knoop is more commonly used in the ceramics community. These WC-Co materials were being compared to a variety of ceramics as part of a larger study. Using Knoop indentation enabled a direct hardness comparison with ceramics.

3mm face of the specimen, then propagating a two-dimensional, sharp precrack using a bridge-flexure fixture. Previous research [46] has shown that a notch is better at developing the precrack in WC-Co. As a result, a straight notch, 0.5mm deep, was created using electrical discharge machining (EDM) with a 0.2mm diameter brass wire. Eight fracture toughness specimens were tested for each material.

3.3 Fractography, Weibull Analysis, & Strength-Size Scaling

Fractographic analysis of the fracture surfaces was conducted to identify the strength-limiting flaws for each material. Optical and scanning electron microscopy were used concurrently to locate and identify the strength-limiting features in both the flexure and tensile specimens, respectively, according to the guidelines outlined in ASTM C1322 [51]. Optical fractography was conducted on all of the tested specimens using a stereoscope to determine the general location and approximate identity of the fracture origin. The test specimens were then batched by predicted flaw type based upon the results of the optical investigation. Select specimens were then acutely investigated using a SEM to specifically identify and characterize the strength-limiting flaws. Weibull analysis, per the recommendations in ASTM C1239 [52], was performed on the strength data generated for each material. Weibull analysis relies on a “weakest link” theory [53, 54], which is applicable in this case due to the tested specimens failing from a single strength-limiting feature. The results of the Weibull analysis were conjoined with the fractography results to garner a wider perspective on the fracture behavior of these materials, and the Weibull statistics were used to describe the strength distributions.

4.0 RESULTS AND DISCUSSION

4.1 Density, Elastic Properties & Microstructures

The average density, elastic properties and sound speeds of each of the four tungsten carbide-cobalt materials are presented in Table 2. The data indicates subtle variations between the four materials, yet these differences are relatively trivial despite the substantial variances in the microstructures. The differences in grain size between each of the materials is apparent from the microstructures in Figure 2. The grain size distribution in CTF24F (Fine) (Figure 2A) appears to be a bit more uniform than the other three materials, which tend to show a bimodal mix of coarse and fine grains, with the coarse grains being about twice the size of the fine grains. This could be attributed to the fact that CTF24F (Fine) does not contain any additives to the binder, such as the VC and Cr_3C_2 in CTS23H (Submicron) and TSF44h5 (Ultrafine) (Table 1), which are utilized to inhibit grain growth during sintering.

Table 2. Average density and elastic properties for each of the four materials.

Material	Density [g/cc]	Elastic Modulus [GPa]	Shear Modulus [GPa]	Bulk Modulus [GPa]	Poisson's Ratio	Longitudinal Wave Speed [m/s]	Shear Wave Speed [m/s]
CTF24F (Fine)	14.3	562	229	344	0.24	6754	4011
CTS23H (Submicron)	14.2	561	226	359	0.23	6810	3985
TSF44h5 (Ultrafine)	14.0	563	226	365	0.24	6841	3985
S105	14.1	585	238	366	0.23	6884	3728

4.2 Mechanical Properties

A summary of the mechanical properties for the four tungsten carbide-cobalt materials is presented in Table 3. The plus/minus values listed in the table represent one standard deviation from the mean for each average value.

Table 3. Summary of the mechanical properties investigated for the four WC-Co materials.

Material	Knoop Hardness, HK ₂ [GPa]	Flexure Strength, σ_{flex} [MPa]	Tensile Strength, σ_{tens} [MPa]	Fracture Toughness, K _{Ic} [MPa-m ^{1/2}]
CTF24F (Fine)	14.2 ± 0.3	2581 ± 131	1944 ± 486	11.3 ± 0.5
CTS23H (Submicron)	15.9 ± 0.3	3058 ± 183	2628 ± 581	8.7 ± 0.3
TSF44h5 (Ultrafine)	17.2 ± 0.3	2760 ± 511	2728 ± 294	7.3 ± 0.1
S105	15.6 ± 0.2 [46]	3099 ± 166	2659 ± 301	10.2 ± 0.5 [47]

4.3 Fractography

Optical fractography was sufficient to understand the fracture behavior of each specimens and the fracture mirror and the fracture origin were clearly defined and easy to observe on the fracture surface of all specimens (Figure 3). However proper identification of the strength-limiting flaw required SEM examination. The fractographic observations of each material are provided in the next sections.

4.3.1 CTF24F (Fine) Specimens

4.3.1.1 Flexure

All 30 flexure specimens for CTF24F (Fine) failed from a large grain, either in the form of a single, immense inclusion more than an order of magnitude larger than the carbide grain size (19 specimens), or a cluster of grains where the individual grains were about two to three times larger than the nominal average grain size (11 specimens). These strength-limiting features were spatially distributed in the volume and at the surface of the specimens. The inclusions were in the form of large singularities, which were identified as WC via energy-dispersive X-ray spectroscopy (EDS) analysis. These particles were irregularly shaped and ranged in size from 15 to 50 μm in any given dimension (see Figure 4A and Figure 4B). Upon closer inspection, these particles exhibited fracture features on their surfaces, indicating that they fractured off a larger piece of material. Additionally, there was a clear and distinct boundary between the inclusion and the normal microstructure. Due to the size of the WC grain and fracture markings on it, these inclusions are likely a contaminant from the powder processing and not a result of abnormal grain growth during sintering. The inclusions were likely introduced during the milling process when WC milling media were used to either refine the grain size of the starting powder or homogenize the carbide and cobalt powders prior to sintering. The other type of large grain fracture origin was a cluster of large grains that were typically about 50 μm in diameter, with the grains within the cluster averaging about 10 μm (see Figure 4C), over five times larger than the nominal grain size of the material (1.85 μm). Again, EDS was used to confirm that these clusters were of the same composition as the rest of the material. These flaws are attributed to abnormal grain growth of the carbide grains during sintering, either due to a lack of grain-refining phases in the local area or preferential alignment of low energy crystal planes, which increases the tendency to form large grains via diffusion [55-58].

4.3.1.2 Tensile

Of the 13 tensile specimens tested for CTF24F (Fine), nine were found to have failed from volume-distributed clusters of porosity ranging from approximately 30 to 100 μm in size (see Figure 5A). Of this subset, two failure origins were a combination of a porous region with a singular, large grain inclusion, similar in appearance to those found in the flexure specimens. The inclusions again appeared to be a brittle particle with highly angular geometries ranging from approximately 75 to 150 μm in size (see Figure 5B), well above the nominal grain size of the material. Again, these inclusions displayed fracture markings indicating that they may have

fractured off the milling media. The remaining four specimens were determined to have failed from machining cracks at the specimen surface.

4.3.2 CTS23H (Submicron) Specimens

4.3.2.1 Flexure

The majority of the CTS23H (Submicron) flexure specimens (25 of 30) failed due to porous regions. SEM inspection revealed clusters (approximately 15 to 20 μm in diameter) of enlarged grains (average grain size of 3 μm) in the areas surrounding several of these flaws (see Figure 6), indicating that the flaws are likely pores that formed during processing. These porous regions could lead to abnormal grain growth during sintering due to the lack of binder phase and grain growth inhibitors, hence the large grain clusters found in the same vicinity. The remaining five specimens were noted to have fracture origins of large grain clusters, similar in appearance to those of CTF24F (Fine), however, porosity was not noted to be as prevalent in the vicinity of these flaws.

4.3.2.2 Tensile

One of the sixteen tensile specimens tested for CTS23H (Submicron) experienced a misalignment during testing, and the specimen failed at an extremely low load value in a bending manner, so this data point and specimen were discarded from any further analysis. However, similar to the dominant flaw found in the CTF24F (Fine) tensile specimens, ten of the remaining specimens were found to have failed from a porous region. The porous regions varied in size from approximately 5 to 40 μm in diameter (see Figure 7A). A single specimen was identified as failing from a large WC grain inclusion, again similar in appearance to the inclusions observed in CTF24F (Fine), though this time the inclusion was measured at only 10 μm in size (see Figure 7B). The final five specimens were identified as failing due to surface-distributed machining cracks (see Figure 7C and D).

4.3.3 TSF44h5 (Ultrafine) Specimens

4.3.3.1 Flexure

The TSF44h5 (Ultrafine) flexure specimens exhibited two different flaw populations, this time with respective spatial distributions. The majority (22 of 30) of the specimens failed due to a porous region (see Figure 8A), similar in appearance to those of the previous materials. These porous regions were spatially distributed at both the surface and in the volume of the test specimen. The porous regions appear to be due to a lack of densification of the material during sintering, as several abnormally large grains (approximately 1.5 μm) were typically observed in

the region surrounding the porosity (see Figure 8B). The other eight specimens failed due to machining cracks at the specimen surface. These specimens were obtained from a different facility than the first two Ceratizit materials, and were noted to have a different surface finish as previously stated and chips were noticed on the specimen surface in the area of surface-distributed fracture origins, Figure 8C.

4.3.3.2 Tensile

Thirteen of the sixteen TSF44h5 (Ultrafine) tensile specimens were classified as failing from volume-distributed flaws of either porosity, a cluster of large grains, or, most commonly, a combination of the two. The porosity was either in the form of a 2-dimensional porous seam (Figure 9A) or a 3-dimensional porous region (Figure 9B). The large grain clusters resided in the porosity and were nominally 10 μm in diameter, while the size of the individual grains ($\approx 2 \mu\text{m}$) that made up the cluster were about five times larger than the nominal grain size of the material (0.4 μm). This grain growth is attributed to a processing-induced flaw, likely where there was an area deficient of cobalt, resulting in carbide-carbide interfaces across which diffusion allowed grain growth to occur during the sintering process [27, 58]. Three specimens were identified as failing from surface-distributed machining cracks.

4.3.4 S105 Specimens

4.3.4.1 Flexure

The comparison material, Kennametal S105, had fracture origins very similar to the three Ceratizit materials. Of the 20 flexure specimens, it was an almost evenly split between two volume-distributed flaw populations, inclusions and porous regions. The inclusions again were in the form of singular large particles identified as WC that appear to be artifacts of the milling process (see Figure 10), though they were a bit smaller in size (approximately 5 to 10 μm) than the inclusions observed in the other materials. The porous regions were typically 15-20 μm in diameter.

4.3.4.2 Tensile

A minor fraction (4 of 20) of the S105 tensile specimens failed from surface-distributed flaws in the form of machining damage. Of the remaining 16 specimens with volume-distributed flaws, six failed from an inclusion and the other ten failed from regions of porosity. The appearance of the inclusions was very similar to the previous inclusions (see Figure 11A), and they were again confirmed as WC particles that ranged in size from 5 to 50 μm . The regions of porosity were an average of 25 μm in diameter (see Figure 11B).

Klünsner and colleagues reported uniaxial tensile strength values for 10 different WC materials fabricated by Ceratizit including three materials containing 12% Co and one with 11.8% Co [59]. These four materials had listed grain sizes and HV30 values very similar to the three materials examined in this study. The tensile strength was obtained using a reduced-gage section specimen that subjected approximately 340mm³ of material to the tensile load, which is more than twice the volume (141mm³) of the specimen used in this effort (Figure 1). Even with this difference in specimen volume the tensile strengths reported [59] are similar to those reported in this effort. All of the observed fracture-initiation flaws identified in this study agree with results on other WC-Co materials investigated via similar fractography analyses [60-63].

4.4 Weibull Analysis

The following Weibull analysis was conducted assuming a two-parameter Weibull distribution using a maximum likelihood estimation (MLE) regression algorithm, following the procedures outlined in ASTM C1239 [52]. The Weibull parameters of Weibull modulus (m) and characteristic strength (σ_θ) are calculated with 90% confidence bounds (as noted in the parentheses) and presented in Table 4, along with the number of specimens tested, mean strengths (plus/minus one standard deviation), and effective volumes (V_e) for future strength-size scaling exercises. The Weibull modulus was unbiased from the number of specimens tested according to the procedures outlined in ASTM C1239.

Table 4. Estimates of the Weibull parameters for the four materials for both testing conditions.

Material	Flexure					Tension				
	#	σ_{mean} (MPa)	m^*	σ_θ^* (MPa)	V_e (mm ³)	#	σ_{mean} (MPa)	m^*	σ_θ^* (MPa)	V_e (mm ³)
CTF24F (Fine)	30	2581 ±133	23.4 (19.4, 31.1)	2639 (2606, 2674)	3.5	13	1944 ±486	13.3 (10.2, 24.5)	2203 (2124, 2285)	141.4
CTS23H (Submicron)	30	3058 ±186	18.0 (15.0, 23.8)	3143 (3091, 3196)	5.1	15	2628 ±581	10.1 (7.9, 17.6)	2924 (2790, 3063)	141.4
TSF44h5 (Ultrafine)	30	2760 ±520	5.7 (4.7, 8.0)	2845 (2677, 3024)	24.7	16	2728 ±294	14.2 (10.9, 23.3)	2850 (2766, 2937)	141.4
S105	20	3099 ±166	20.7 (16.7, 29.7)	3174 (3119, 3230)	3.9	20	2659 ±301	13.6 (10.9, 19.8)	2762 (2692, 2835)	141.4

*Note: 90% confidence intervals are included in parentheses

The plots of the Weibull analysis for each of the four materials in both loading conditions are presented in Figure 12. Some careful considerations were made when performing the Weibull analysis in conjunction with the results of the fractography investigations. An allowance, per ASTM C1239 [52], is to censor a minor flaw population, to simplify the analysis, if it had minimal impact on the Weibull parameters. An example of this is the surface-distributed machining

flaws noted for the TSF44h5 (Ultrafine) flexure specimens, or the five (of thirty) CTS23H (Submicron) specimens that had a fracture origin in the form of volume-distributed large grain cluster. To confirm this assumption, the flaw populations were segregated and Weibull parameters were calculated separately to ensure the minor population did not have a pronounced effect on the overall Weibull statistics. Similarly, if a specimen set had two, distinct major flaw populations then they were analyzed independently and as one set to determine whether it would be appropriate to combine the two populations into a single population for simplification of the analysis. This situation can be observed in the flexure specimens of CTF24F (Fine). Weibull analysis was performed on the two populations (inclusions and large grain clusters) separately and they were found to have extremely similar Weibull parameters with largely overlapping confidence bounds, [inclusions: $m = 24.2$ (17.8, 33.2) and $\sigma_\theta = 2619$ (2576, 2663) and large grains: $m = 21.1$ (13.9, 32.6) and $\sigma_\theta = 2670$ (2604, 2738)] therefore they were treated as one population for the overall analysis. In addition, the two flaw types were approximately 50 μm in largest dimension, rendering them as equivalent flaw sizes when undergoing loading, which helps to support the previous assumption and findings of similar Weibull behavior for the two separate flaw populations. This same approach was taken for the S105 flexure and tensile specimen sets, possessing major flaw populations of inclusions and porous regions.

4.5 Density, Elastic and Mechanical Properties

All four materials had density values comparable to the company literature values and each exhibited nominally equivalent elastic properties (Table 2). The similarities in the elastic properties were to be expected given their similar compositions. However, the differences in microstructure begin to emerge and have a greater influence when comparing the mechanical properties (Table 3). Although the Knoop hardness values measured in this effort could not be directly compared to the company provided Vickers hardness values, the trend in hardness was consistent with the ultrafine grain size (TSF44h5) being the hardest. Conversely, the coarser grained CTF24F had the highest fracture toughness. In general, three anticipated trends were observed and are presented in Figure 13: (A) Hardness decreasing with increasing grain size, (B) toughness increasing with increasing grain size, and (C) inverse relationship between hardness and toughness.

A finer carbide grain size is attributed to a higher hardness, due to a Hall-Petch relationship. However, toughness decreases with grain size, as the energy needed for a crack to propagate around these smaller grains is much lower, leading to a lower degree of tortuosity in the crack

path. The three Ceratizit materials exhibited the anticipated trends in properties due to their varying grain sizes, but similar binder content, while the S105 material did not conform to these trends. This is likely due to the broad characterization of carbide grain size “classes” or “families”. If the “submicron” grain size of the S105 material were to shift more towards the upper limit of 0.8 μm , the hardness and toughness versus grain size trends would likely hold true for all four materials.

The CTS23H (Submicron) material possessed the closest property values to the comparison material (S105), mainly attributed to their similar grain size. Although it has a lower binder content, the S105 had a higher toughness and lower hardness than the CTS23H (Submicron). Therefore, the different additives must account for the variations between the two materials. The VC and Cr_3C_2 provide hardening contributions to the CTS23H (Submicron), while the Cr additive to the S105 enhances the toughness of the material.

The TSF44h5 (Ultrafine) material exhibited a high variation in flexure strength properties, which is attributed to a combination of different flaw populations. These materials came from a different Ceratizit manufacturing facility, as noted previously, and did not appear to have the same surface finish as the other two Ceratizit materials. This difference in finish may indicate that the grinding process employed to achieve the specified rod diameter was different than the process used on the CTF24F (Fine) and CTS23H (Submicron). Fractographic analysis revealed this was the only material where the flexure specimens exhibited a substantial population of surface-distributed machining flaws (7/30). In addition, fractography determined that the flaws in this material appear to be much smaller than the other materials. Both of these factors will contribute to the large spread in flexure strength. The fracture toughness values generated using the single-edge precracked beam specimen and those calculated from the measured flaw size and strength values, in accordance with linear elastic fracture mechanics, are in excellent agreement (see Table 5).

With the exception of the TSF44h5 (Ultrafine), the flexure strength of the other three WC-Co materials is a few hundred megapascals higher than the uniaxial flexure strength. This is not unexpected due to the vast difference in the amount of material interrogated by the two different specimens under the associated loading configurations. Previous studies [6, 64, 65, 66, 67] have shown that a residual compressive stress, ranging from a few hundred megapascals to 2-3 GPa, can develop at the surface of WC-Co materials due to the machining/grinding processes used to achieve dimensional specifications. While such stresses were not measured

as part of this effort, the authors do not believe that any residual surface stresses that might be present in these four WC-Co materials had an influence on the flexure strength. Further supporting this is the fracture toughness data in **Table 5**. The fracture toughness values calculated from fracture mechanics, using the measured flexure strength and the size of the strength-limiting flaw, are in excellent agreement with the fracture toughness determined by the SEPB method. If the residual compressive stress had an influence the flexure strength values would be higher, which would result in the calculated fracture toughness values for the flexure specimens being higher than the SEPB values.

Table 5. Results of analysis of the flaw size (calculated and measured), mirror radius, fracture toughness (calculated from predicted flaw size and experimentally measured), and mirror constant.

Material	Loading	Flaw size, c (μm)		Mirror radius, R (μm)	Mirror:Flaw Ratio, R/c	Fracture toughness, K_{Ic} ($\text{MPa}\cdot\text{m}^{1/2}$)		Mirror constant, A ($\text{MPa}\cdot\text{m}^{1/2}$)
		Calc.	Meas.			Calc.	Exp. (SEPB)	
CTF24F (Fine)	FLEX	12 \pm 2.4	16 \pm 6.2	100 \pm 38	6.3	11.8 \pm 2.0	11.3 \pm 0.5	26 \pm 4.6
	TENS	33 \pm 31	40 \pm 8.8	244 \pm 194	6.1	14.0 \pm 1.0		26 \pm 3.2
CTS23H (Submicron)	FLEX	4.8 \pm 0.6	7.2 \pm 1.9	52 \pm 11	7.2	9.9 \pm 1.2	8.7 \pm 0.3	22 \pm 2.3
	TENS	9.2 \pm 6.5	14 \pm 9.2	78 \pm 48	5.6	11.0 \pm 2.7		20 \pm 3.6
TSF44h5 (Ultrafine)	FLEX	4.6 \pm 2.0	5.0 \pm 1.4	55 \pm 13	11.0	7.1 \pm 2.8	7.3 \pm 0.1	21 \pm 2.6
	TENS	5.4 \pm 1.5	13 \pm 4.7	64 \pm 22	4.9	11.0 \pm 1.4		21 \pm 2.9
S105	FLEX	7.6 \pm 0.8	10 \pm 1.6	30 \pm 10	3.0	11.7 \pm 3.6	10.2 \pm 0.5	17 \pm 2.0
	TENS	12 \pm 2.7	13 \pm 4.0	37 \pm 13	2.8	10.6 \pm 1.8		16 \pm 2.7

4.6 Fractography and Weibull Analysis

The lack of a consistent flaw population from flexure to tensile testing for the three Ceratizit materials did not allow for overarching conclusions about the strength based on differences in grain size. This variation in flaw population is also concerning in relation to the manufacturing of the materials. The flexure and tensile specimens were produced from two different diameter rods. The rods used to machine the tensile strength specimens had a diameter over two-and-a-half times larger than the rods for the flexure specimens. Since these rods are typically formed via an extrusion process, there is an inherent pressure gradient between the surface and the center of the rods. This pressure gradient likely accounts for the increased tendency for porosity to form in the center portion of the larger diameter extruded rod, which results in failure from porosity in the tensile strength specimens, while the flexure strength specimens more commonly failed from an inclusion or large grain cluster, though there was still some

porosity present. The manufacturer indicates that their materials are sintered but sometimes pressure is added. Even after a sinter-hot isostatic press (HIP) procedure, there is likely still some residual internal porosity that cannot be driven out of the material, which can be observed in the density values for the materials (Table 2) lying a few percent below the theoretical density value (composition and unspecified/unaccounted for additives can also play a role). Additionally, there is the possibility that batch-to-batch variability played a role. This is highlighted by the significant difference in the strength-limiting flaw population between the flexure (WC inclusion and large WC grains) and tension (porosity) specimens of the CTF24F (Fine) material.

The Weibull analysis in Figure 12 appears largely appropriate for the analysis of the CTF24F (Fine), CTS23H (Submicron), and S105 materials for the two separate loading conditions, even though the flaw population was not consistent for the former two. The S105 cermet was the only material that showed consistent strength-limiting flaws between flexure and tensile testing. The Weibull analysis of TSF44h5 (Ultrafine) was highly inconsistent, similar to the majority of the mechanical property analysis for the same material. Much of this inconsistency in flexure strength is attributed to machining damage from the surface finishing process, and the susceptibility of a relatively homogeneous, ultra-fine-grained microstructure to large variations in fracture-dependent property. This can be observed in the extremely low Weibull modulus for the flexure specimens of this material, as well as the large deviations in individual data points to the Weibull fit line, compared to the other three materials. However, the Weibull analysis of the tensile specimen datasets was relatively consistent across the four materials. The various Weibull moduli (Table 5) were relatively consistent within the individual loading conditions, aside from the aforementioned TSF44h5 (Ultrafine) flexure results, and are in decent agreement with similar specimens previously evaluated [27]; however, the values are generally lower than previously observed. This is likely due to the difference in surface finish of the flexure specimens (as-ground vs mirror-like [27]), which could reduce the effect of surface-distributed flaws and the interaction of sub-surface, volume-distributed flaws by machining damage on the surface of the specimen.

A previous study [68] has shown that the ratio of the inner fracture mirror radius to the fracture origin size is approximately 6:1 for polycrystalline ceramics but values as low as three (3) and as high as ten (10) were reported. The ratio for both the flexure and tensile specimens of the CTF24F (Fine) and CTS23H (Submicron) are in excellent agreement with this 6:1 ratio. The

values for the TSF44h5 (Ultrafine) and S105 deviate from this ratio but are within or very close the range of values previously reported for polycrystalline ceramics.

The fracture mirror size is related to the stress at the fracture origin according to the relationship: $\sigma\sqrt{R} = A$, where σ is the tensile stress at the origin, R is the radius of the fracture mirror, and A is the fracture mirror constant. The radius of the fracture mirror was measured on the fracture surface of each specimen and was coupled with the tensile strength of the respective specimen generating a plot of σ versus inverse square root of the mirror radius. The slope of this line is the fracture mirror constant. The mirror constant for each WC (see Table 5) was consistent whether it was determined by measuring the mirror size on the fracture surface of flexure or tensile strength specimens. These values were also in general agreement with previously reported fracture mirror constants for WC materials [69].

5.0 CONCLUSION

Three tungsten carbide-cobalt materials from a single company, with similar binder content, but varying grain sizes, were obtained and evaluated for comparison to a tungsten carbide with a similar Co content but produced by a different manufacturer. The tungsten carbide grain sizes and overall microstructure of each material were quite different; however, these differences did not extend to elastic properties. Subtle differences in the mechanical property values of hardness, flexure strength, tensile strength, and fracture toughness as a function of tungsten carbide grain size were observed. In general, an increase in hardness and tensile strength with decreasing grain size was observed, as was an increase in fracture toughness with increasing grain size. However, the flexure strength results did not show high correlation to grain size due to variations in the strength-limiting features in these specimens. The S105 material was found to be most similar in properties to CTS23H (Submicron) due to their similar grain size. Overall, there was no observable trend in performance across multiple mechanical properties with changing microstructure. Rather, it appears that a combination of grain size and composition (of both binder and other additives) must be considered when selecting a cermet material for a specific desired performance metric.

Fractography and Weibull analyses were performed on all four materials. On the whole, Weibull analysis is appropriate for evaluating the failure probability of these composite materials. However, due to variations in strength-limiting flaw populations, as determined from fractography, it is difficult to garner broad conclusions about the failure behavior. These flaw population differences are likely due to pressure gradients in the extrusion process of different

diameter rods and are also sensitive to the machining procedure used to achieve the final rod diameter the test specimens.

ACKNOWLEDGEMENTS

This research was supported in part by an appointment to the Postgraduate Research Participation Program at the U.S. Army Research Laboratory administered by the Oak Ridge Institute for Science and Education through an interagency agreement between the U.S. Department of Energy and U.S. ARL (Pittari). Additional support was provided by UIC TS, Bowhead Science and Technology, LLC (Wright) and the Army Research Laboratory College Qualified Leaders (CQL) Program administered by the Academy of Applied Science (Atwater).

REFERENCES

1. Waldorf, D., Liu, S., Stender, M. and Norgan, D., *Alternative Binder Carbide Tools for Machining Superalloys*. in *ASME 2008 International Manufacturing Science and Engineering Conference collocated with the 3rd JSME/ASME International Conference on Materials and Processing*. 2008. American Society of Mechanical Engineers.
2. Schubert, W.-D., E. Lassner, and W. Böhlke, *Cemented Carbide-a Success Story*. ITIA Newsletter June, 2010.
3. Sandvik Coromant, *Modern metal cutting: a practical handbook*. 1994: Sandvik Coromant.
4. Schubert, W.D., Fugger, M., Wittman, B. and Useldinger, R., *Aspects of sintering of cemented carbides with Fe-based binders*. International Journal of Refractory Metals and Hard Materials, 2015. **49**: p. 110-123.
5. Schubert, W., Neumeister, H., Kinger, G., and Lux, B., *Hardness to toughness relationship of fine-grained WC-Co hardmetals*. International Journal of Refractory Metals and Hard Materials, 1998. **16**(2): p. 133-142.
6. O'Quigley, D.G.F., S. Luyckx, and M.N. James, *New results on the relationship between hardness and fracture toughness of WC-Co hardmetal*. Materials Science and Engineering: A, 1996. **209**(1-2): p. 228-230.
7. Dobrzański, L. and B. Dołżańska, *Hardness to toughness relationship on WC-Co tool gradient materials evaluated by Palmqvist method*. Archives of Materials Science and Engineering, 2010. **43**(2): p. 87-93.
8. Cardarelli, F., *Materials handbook: a concise desktop reference*. 2008: Springer Science & Business Media.
9. Kurlov, A.S. and A.I. Gusev, *Tungsten carbides*. Springer Ser. Mater. Sci, 2013. **184**: p. 34-6.
10. Carbide, G., *The designer's guide to Tungsten Carbide*. General Carbide Corp, Greensburg.[online] www.generalcarbide.com. [accessed at 29 November 2014], 2008.
11. Wilburn, D.R., *Cobalt mineral exploration and supply from 1995 through 2013*. 2011, US Geological Survey.
12. Shedd, K.B., E.A. McCullough, and D.I. Blalwas, *Global trends affecting the supply security of cobalt*, in *Mining Engineering*. 2017. p. 37-42.
13. Donachie, M.J. and S.J. Donachie, *Superalloys: a technical guide*. 2002: ASM international.
14. Campbell, F.C., *Elements of metallurgy and engineering alloys*. 2008: ASM International.
15. Davis, J., *Alloying. Understanding the Basics*, ASM International, Materials Park, OH, 2001: p. 44073-0002.
16. Exner, H.E., *Physical and chemical nature of cemented carbides*. International Metals Reviews, 1979. **24**(1): p. 149-173.
17. Gille, G., Bredthauer, J., Gries, B., Mende, B., and Heinrich, W., *Advanced and new grades of WC and binder powder – their properties and application*. International Journal of Refractory Metals and Hard Materials, 2000. **18**(2-3): p. 87-102.
18. Engel, U. and H. Hübner, *Strength improvement of cemented carbides by hot isostatic pressing (HIP)*. Journal of materials science, 1978. **13**(9): p. 2003-2012.

19. North, B., Greefield, M.S., McCoy, W.C. and Vankirk, J.S., *Effect of pressure sinter and post-treatment on the strength of cemented carbide*. Advances in Powder Metallurgy and Particulate Materials, Vol 8, 111-123 (1992)
20. Jia, K., T.E. Fischer, and B. Gallois, *Microstructure, hardness and toughness of nanostructured and conventional WC-Co composites*. Nanostructured Materials, 1998. **10**(5): p. 875-891.
21. Mi, S. and T. Courtney, *Synthesis of WC and WC-Co cermets by mechanical alloying and subsequent hot isostatic pressing*. Scripta materialia, 1998. **38**(1): p. 171-176.
22. Richter, V. and M. Ruthendorf, *On hardness and toughness of ultrafine and nanocrystalline hard materials*. International Journal of Refractory Metals and Hard Materials, 1999. **17**(1-3): p. 141-152.
23. Michalski, A. and D. Siemiaszko, *Nanocrystalline cemented carbides sintered by the pulse plasma method*. International Journal of Refractory Metals and Hard Materials, 2007. **25**(2): p. 153-158.
24. Sivaprahasam, D., S.B. Chandrasekar, and R. Sundaresan, *Microstructure and mechanical properties of nanocrystalline WC–12Co consolidated by spark plasma sintering*. International Journal of Refractory Metals and Hard Materials, 2007. **25**(2): p. 144-152.
25. Deorsola, F.A., Vallauri, D., Ortigoza Villalba, G.A., and De Benedetti, B., *Densification of ultrafine WC–12Co cermets by pressure assisted fast electric sintering*. International Journal of Refractory Metals and Hard Materials, 2010. **28**(2): p. 254-259.
26. Bonache, V., Slavador, M.D., Busquets, D., Burguete, P., Martinez, E., Spaiña, F., Sánchez, G., *Synthesis and processing of nanocrystalline tungsten carbide: towards cemented carbides with optimal mechanical properties*. International Journal of Refractory Metals and Hard Materials, 2011. **29**(1): p. 78-84.
27. Tarragó, J.M., Coureaux, D., Torres, Y., Jiménez-Piqué, E. Schneider, L., Fair, J. and Llanes, L., *Strength and reliability of WC-Co cemented carbides: Understanding microstructural effects on the basis of R-curve behavior and fractography*. International Journal of Refractory Metals and Hard Materials, 2018. **71**: p. 221-226.
28. Hall, E., *The deformation and ageing of mild steel: III discussion of results*. Proceedings of the Physical Society. Section B, 1951. **64**(9): p. 747.
29. Petch, N., *The cleavage strength of polycrystals*. Journal of the Iron and Steel Institute, 1953. **174**: p. 25-28.
30. Pittari, J.J., Murdock, H., Kilczeewski, S., Hornbuckle, B., Swab, J.J., Darling, K. and Wright, J., *Sintering of tungsten carbide cermets with an iron-based ternary alloy binder: Processing and thermodynamic considerations*. International Journal of Refractory Metals and Hard Materials, 2018.
31. Liu, C., *Alternative binder phases for WC cemented carbides*. 2014.
32. Penrice, T., *Alternative binders for hard metals*. Journal of Materials Shaping Technology, 1987. **5**(1): p. 35-39.
33. Toller, L., S. Jacobson, and S. Norgren, *Life time of cemented carbide inserts with Ni-Fe binder in steel turning*. Wear, 2017. **376-377**: p. 1822-1829.
34. Chen, C.-S., Yang, C.-C., Chai, H.-Y., Yeh, J.-W. and Chau, J.L.H., et al., *Novel cermet material of WC/multi-element alloy*. International Journal of Refractory Metals and Hard Materials, 2014. **43**: p. 200-204.

35. Uhrenius, B., H. Pastor, and E. Pauty, *On the composition of Fe-Ni-Co-WC-based cemented carbides*. International Journal of Refractory Metals and Hard Materials, 1997. **15**(1-3): p. 139-149.
36. Wittmann, B., W.-D. Schubert, and B. Lux, *WC grain growth and grain growth inhibition in nickel and iron binder hardmetals*. International Journal of Refractory Metals and Hard Materials, 2002. **20**(1): p. 51-60.
37. Schneider Jr, G., *Chapter 1: Cutting-Tool Materials*. Tooling and Production, 2001.
38. Genga, R.M., Akdogan, G., Polese, B, Garrett, J.C., and Cornish, L., *Abrasion wear, thermal shock and impact resistance of WC-cemented carbides produced by PECS and LPS*. International Journal of Refractory Metals and Hard Materials, 2015. **49**: p. 133-142.
39. Morton, C.W., D.J. Wills, and K. Stjernberg, *The temperature ranges for maximum effectiveness of grain growth inhibitors in WC-Co alloys*. International Journal of Refractory Metals and Hard Materials, 2005. **23**(4-6): p. 287-293.
40. Sun, L., J. Xiong, and Z.X. Guo. *Effects of Nano-Al₂O₃ Additions on Microstructures and Properties of WC-8Co Hard Metals*. in *Advanced Materials Research*. 2010. Trans Tech Publ.
41. Wang, H., T. Webb, and J.W. Bitler, *Different effects of Cr₃C₂ and VC on the sintering behavior of WC-Co materials*. International Journal of Refractory Metals and Hard Materials, 2015. **53**: p. 117-122.
42. Spriggs, G.E., *A history of fine grained hardmetal*. International Journal of Refractory Metals and Hard Materials, 1995. **13**(5): p. 241-255.
43. Almond, E., *Some characteristics of very-fine-grained hardmetals*. Met. Powder Rep., 1987. **42**(7): p. 512.
44. Upadhyaya, G.S., *Materials science of cemented carbides — an overview*. Materials & Design, 2001. **22**(6): p. 483-489.
45. Zackrisson, J., Jansson, B., Uphadyaya, G.S. and Andrén, H.-O., *WC-Co based cemented carbides with large Cr₃C₂ additions*. International Journal of Refractory Metals and Hard Materials, 1998. **16**(4-6): p. 417-422.
46. Swab, J.J. and J.C. Wright, *Application of ASTM C1421 to WC-Co fracture toughness measurement*. International Journal of Refractory Metals and Hard Materials, 2016. **58**: p. 8-13.
47. ASTM International, *Standard Test Method for Knoop Indentation Hardness of Advanced Ceramics*. C1326 (2013), ASTM International: West Conshohocken, PA.
48. ASTM International, *Standard Test Method for Flexural Strength of Advanced Ceramics at Ambient Temperature--Cylindrical Rod Strength*. C1634 (2018), ASTM International: West Conshohocken, PA.
49. ASTM International, *Standard Test Method for Tensile Strength of Monolithic Advanced Ceramics at Ambient Temperatures*. C1273 (2018), ASTM International: West Conshohocken, PA.
50. ASTM International, *Standard Test Methods for Determination of Fracture Toughness of Advanced Ceramics at Ambient Temperature*. C1421 (2009), ASTM International: West Conshohocken, PA. p. 624-655.

51. ASTM International, *Standard Practice for Fractography and Characterization of Fracture Origins in Advanced Ceramics*. C1322 (2015), ASTM International: West Conshohocken, PA.
52. ASTM International, *Standard practice for reporting uniaxial strength data and estimating weibull distribution parameters for advanced ceramics*. C1239 (2013), ASTM International: West Conshohocken, PA.
53. Weibull, W., *A Statistical Distribution Function Of Wide Applicability*. Journal of Applied Mechanics, 1951. **18**: p. 293-297.
54. Davies, D. *The statistical approach to engineering design in ceramics*. in *Proceedings of the British Ceramic Society*. 1973.
55. Schubert, W., A. Bock, and B. Lux, *General aspects and limits of conventional ultrafine WC powder manufacture and hard metal production*. International Journal of Refractory metals and Hard materials, 1995. **13**(5): p. 281-296.
56. Sommer, M., Schubert, W., Zobetz, E., Warbichler, P., *On the formation of very large WC crystals during sintering of ultrafine WC-Co alloys*. International Journal of Refractory Metals and Hard Materials, 2002. **20**(1): p. 41-50.
57. Kumar, V., Fang, Z.Z., Wright, S.I. and Nowell, M.M., *An analysis of grain boundaries and grain growth in cemented tungsten carbide using orientation imaging microscopy*. Metallurgical and Materials Transactions A, 2006. **37**(3): p. 599-607.
58. Kim, J.D., S.J.L. Kang, and J.W. Lee, *Formation of Grain Boundaries in Liquid - Phase - Sintered WC-Co Alloys*. Journal of the American Ceramic Society, 2005. **88**(2): p. 500-503.
59. Klünsner, T., Marsoner, S., Ebner, R., Pippan, R., Glätzle, J. and Püschel, A., *Effect of Microstructure on Fatigue Properties of WC-Co Hard Metals*, Proc. Eng., 2, 2001-2010 (2010)
60. Han, D. and J. Mecholsky, *Fracture analysis of cobalt-bonded tungsten carbide composites*. Journal of materials science, 1990. **25**(12): p. 4949-4956.
61. Torres, Y., M. Anglada, and L. Llanes, *Fatigue mechanics of WC-Co cemented carbides*. International Journal of Refractory Metals and Hard Materials, 2001. **19**(4-6): p. 341-348.
62. Cha, S.I., Lee, K.H., Ryu, H.J. and Hong, S.H., *Effect of size and location of spherical pores on transverse rupture strength of WC-Co cemented carbides*. Materials Science and Engineering: A, 2008. **486**(1-2): p. 404-408.
63. Suzuki, H. and K. Hayashi, *The strength of WC-Co cemented carbide in relation to structural defects*. Transactions of the Japan Institute of Metals, 1975. **16**(6): p. 353-360.
64. Cutler, R.A., and Virkar, A.V., *The Effect of Binder Thickness and Residual Stresses on the Fracture Toughness of Cemented Carbides*, J. Mater. Sci. **20** (1985) 3557–3573.
65. Exner, H.E., *The influence of sample preparation on Palmqvist's method for toughness testing of cemented carbides*, Trans. Metall. Soc. AIME **245** (1969) 677–683.
66. Snell, P.O. and Pärnama, E., *The influence of abrasive polishing on the stress state and toughness properties of cemented carbides*, in: H.H. Hausner, W.E. Smith (Eds.), *Modern Developments in Powder Metallurgy*, American Powder Metallurgy Institute, Princeton, NJ 1974, pp. 645–664.

67. French, D.N., X-Ray stress analysis of WC-Co cermets I, procedures, *J. Am. Ceram. Soc.* **52** (5) (1969) 267–271.
68. Mechlosky, Jr., J.J., Freiman, S.W. and Rice, R.W., "Fracture Surface Analysis of Ceramics," *J. Mat. Sci.*, **11** (1976) 1310-1319
69. Luyckx, S.B. and A. Sannino, *Crack branching and fracture mirrors in cemented tungsten carbide*. *Journal of materials science*, 1988. **23**(4): p. 1243-1247.

Figure Captions

Figure 1. Technical drawing of the uniaxial tensile specimen (units: mm; scale 3:2).

Figure 2. Microstructure of the four materials: (A) CTF24F (Fine), (B) CTS23H (Submicron), (C) TSF44h5 (Ultrafine), and (D) S105. Note the slight difference in scale for (D) compared to the other three materials

Figure 3. Optical images of a CTS23H (Submicron) tensile specimen showing the entire fracture surface (A) with the fracture mirror marked by the red arrows. (B) close up of the mirror and origin, the origin is in the center of the mirror and highlighted by the red arrow. The fracture origin in this specimen was a large WC grain

Figure 4. SEM images of representative fracture origins in the CTF24F (Fine) flexure specimens: (A) and (B) are WC inclusions, most likely introduced during processing, while (C) is a cluster of large WC grains at the specimen surface that are the result of abnormal grain growth

Figure 5. Representative SEM images of the fracture origins found in the CTF24F (Fine) tensile specimens: (A) Porous region and (B) WC inclusion. Note the fracture markings (red arrow) on the WC inclusion indicating this might be a piece of a WC milling media that fractured off during power processing

Figure 6. SEM image of one of the porous regions identified as the strength-limiting flaw in the CTS23H (Submicron) flexure specimens. This flaw happened to be located at the specimen surface (i.e., machined surface)

Figure 7. SEM images of the strength-limiting flaws identified from the CTS23H (Submicron) tensile specimens: (A) Porous region, (B) WC inclusion and (C) and (D) Optical image of a machining damage. (C) show the fracture surface with the origin at the surface surrounded by the fracture mirror. Note how the edge is jagged. (D) is a view of the external surface showing many deep longitudinal machining grooves that match with the jagged edge shown in (C)

Figure 8. Representative SEM images of the fracture origins in the TSF44h5 (Ultrafine) flexure specimens: (A) small porous region, (B) larger porous region, the submicron black spots are pores while the larger black features are contamination and (C) optical image of machining damage on the external surface of a specimen that was the fracture origin

Figure 9. SEM images of the strength-limiting flaws associated with the TSF44h5 (Ultrafine) uniaxial tensile specimens: (A) Porous seam with a cluster of large grains and (B) a porous region with a large grain cluster

Figure 10. SEM images of the WC inclusion as the fracture origin in the S105 flexure specimens.

Figure 11. Representative SEM images of the fracture origins identified for the S105 uniaxial tensile specimens: (A) WC inclusion and (B) porous region, all of the black areas are submicron pores.

Figure 12. Plots of the results of Weibull analysis for the four materials considering the loading configuration and fractographically-identified strength-limiting flaw analysis: (A) CTF24F (Fine), (B) CTS23H (Submicron), (C) TSF44h5 (Ultrafine), and (D) S105. Specimen data points from flexure are in blue, while tensile specimens are in red. The corresponding dash-dot fit line is plotted based upon the unbiased

Weibull modulus (m_0) provided in each plot along with the characteristic strength (σ_0) for each loading configuration. Note that the specimens that failed due to machining damage have been censored from the numerical analysis but are included in the plot for completeness.

Figure 13. Plots of: (left) hardness versus grain size, (middle) toughness versus grain size, and (right) hardness versus toughness for the four materials.

NOTE: 1) SURFACE FINISH 0.4 MICRONS ALL OVER EXCEPT END FACES WHICH MAY BE 0.8 MICRONS
 2) FINAL GRIND OF GAGE SECTION TO BE LONGITUDINAL

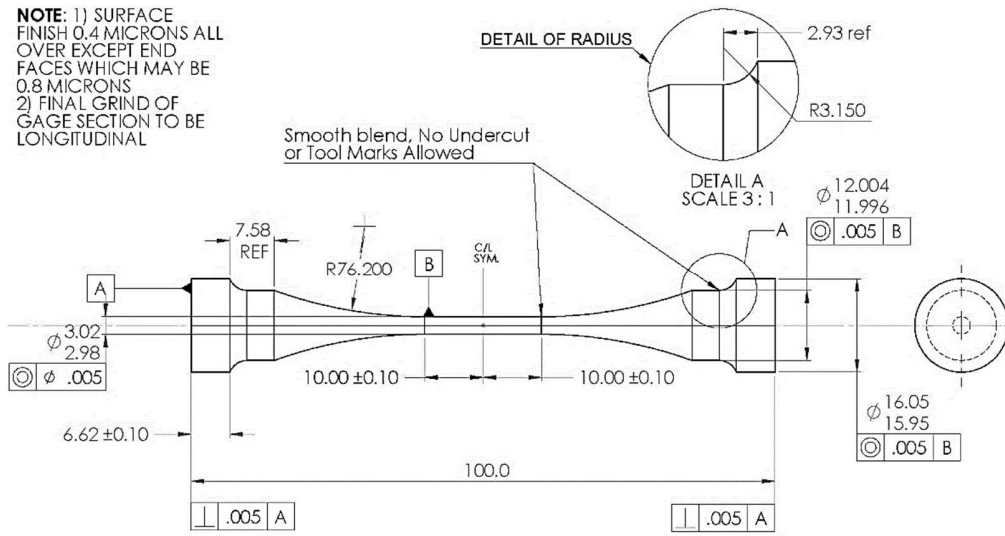


Figure 1. Technical drawing of the uniaxial tensile specimen (units: mm; scale 3:2).

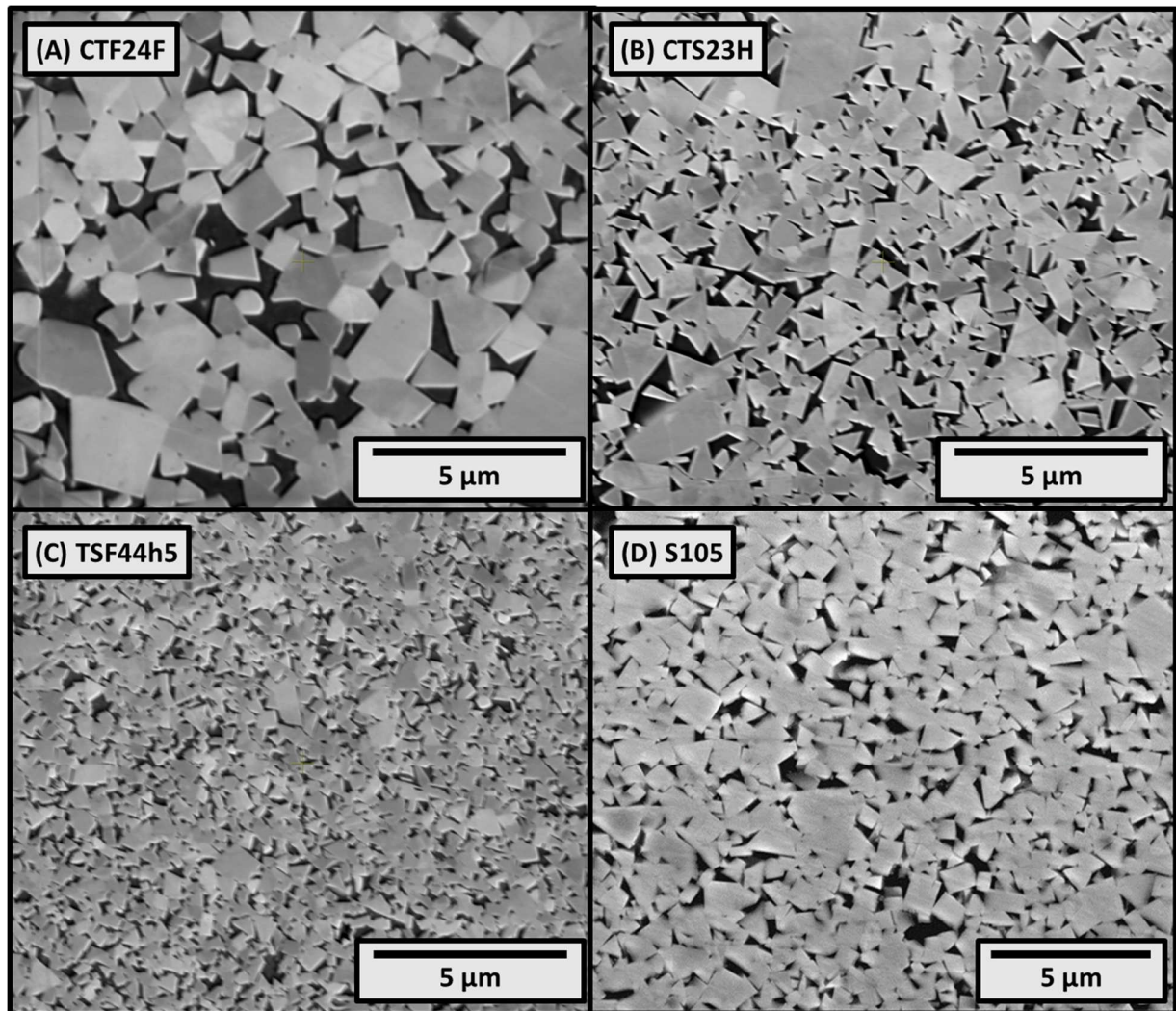


Figure 2. Microstructure of the four materials: (A) CTF24F (Fine), (B) CTS23H (Submicron), (C) TSF44h5 (Ultrafine), and (D) S105. Note the slight difference in scale for (D) compared to the other three materials.

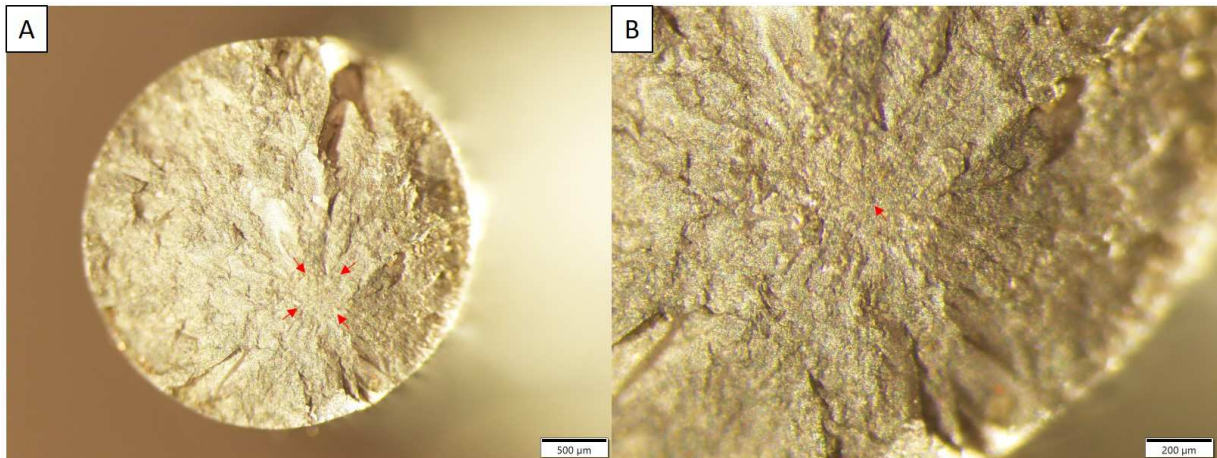


Figure 3. Optical images of a CTS23H (Submicron) tensile specimen showing the entire fracture surface (A) with the fracture mirror marked by the red arrows. (B) close up of the mirror and origin, the origin is in the center of the mirror and highlighted by the red arrow. The fracture origin in this specimen was a large WC grain.

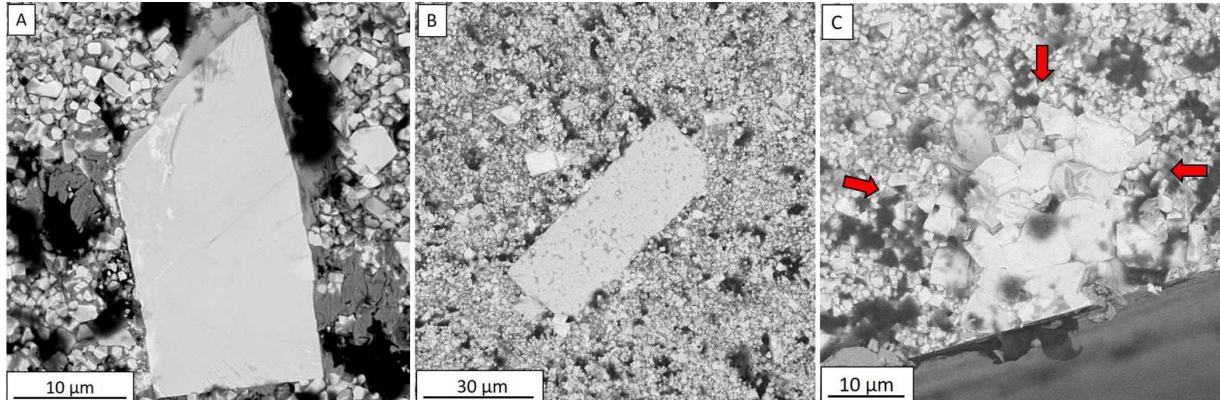


Figure 4. SEM images of representative fracture origins in the CTF24F (Fine) flexure specimens: (A) and (B) are WC inclusions, most likely introduced during processing, while (C) is a cluster of large WC grains at the specimen surface that are the result of abnormal grain growth.

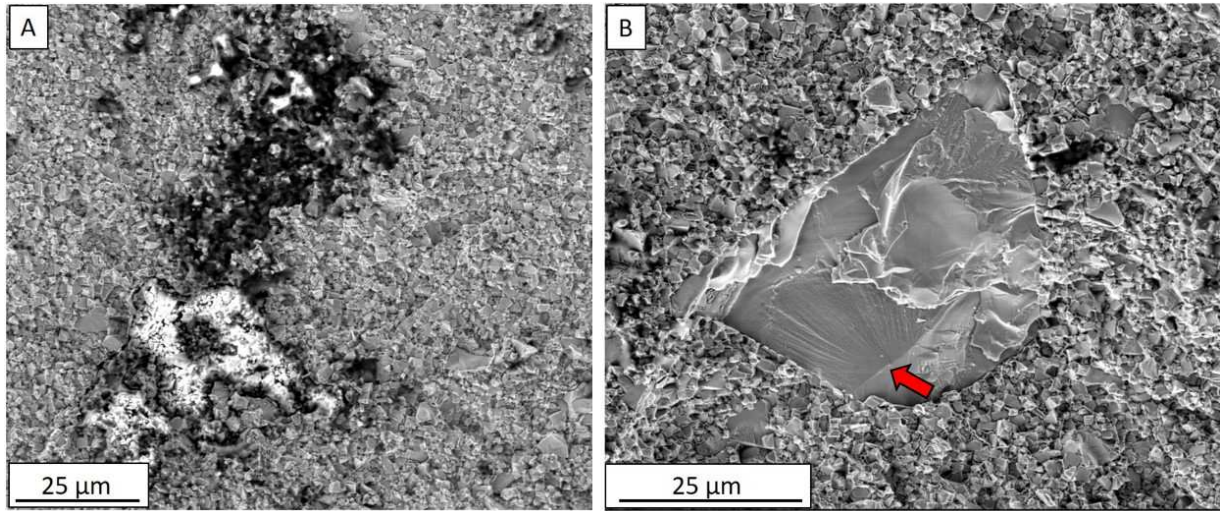


Figure 5. Representative SEM images of the fracture origins found in the CTF24F (Fine) tensile specimens: (A) Porous region and (B) WC inclusion. Note the fracture markings (red arrow) on the WC inclusion indicating this might be a piece of a WC milling media that fractured off during power processing.

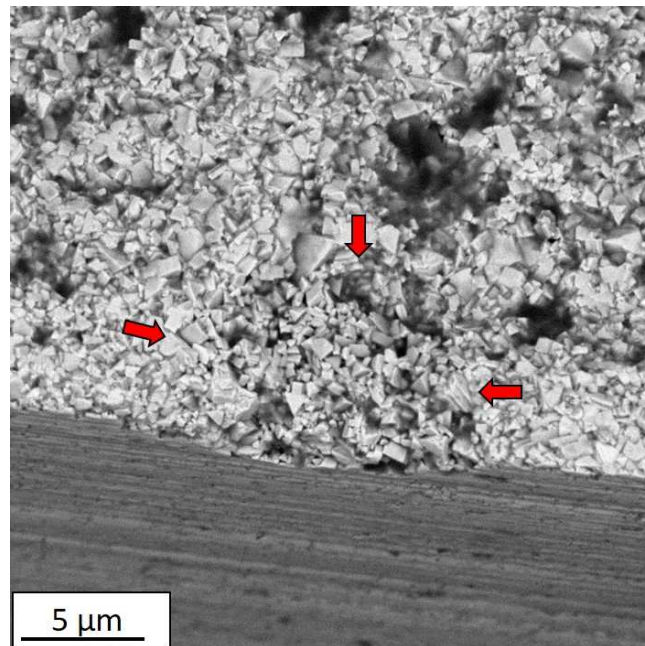


Figure 6. SEM image of one of the porous regions identified as the strength-limiting flaw in the CTS23H (Submicron) flexure specimens. This flaw happened to be located at the specimen surface (i.e., machined surface).

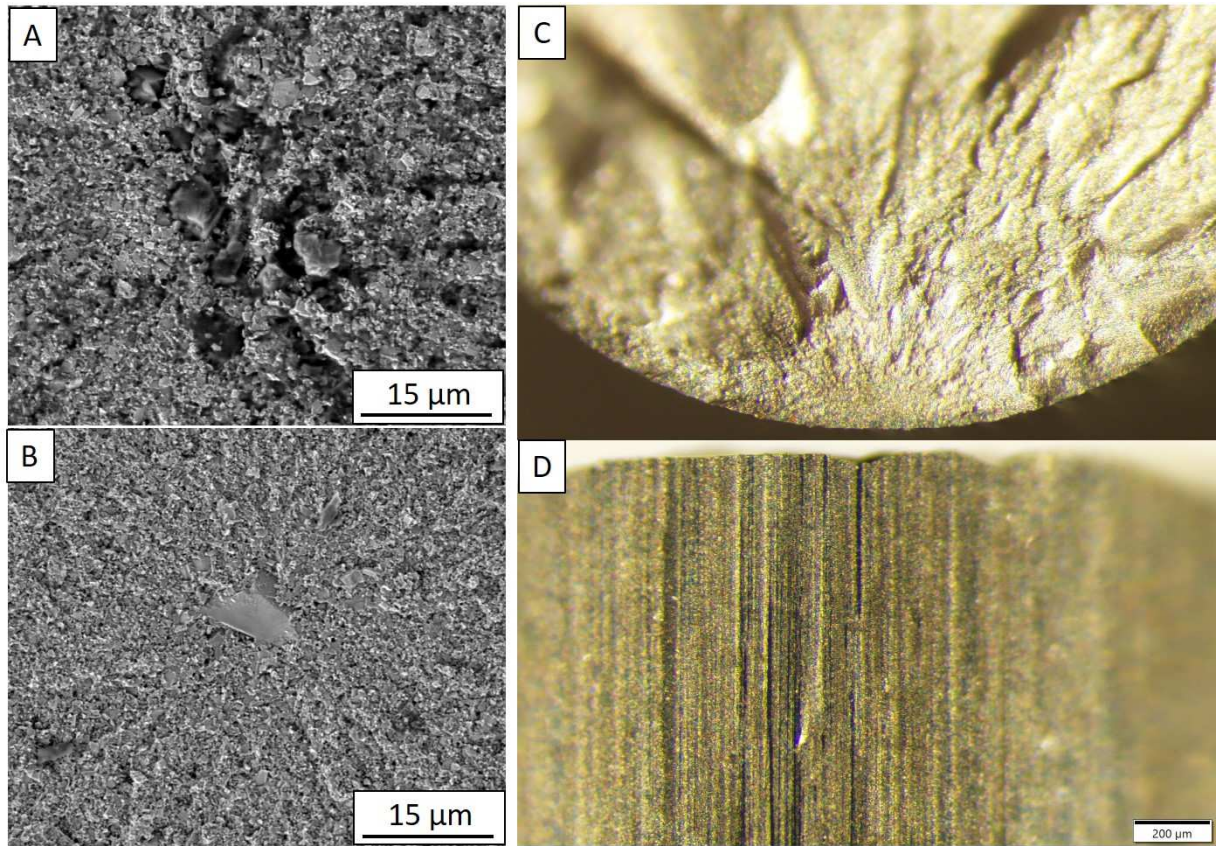


Figure 7. SEM images of the strength-limiting flaws identified from the CTS23H (Submicron) tensile specimens: (A) Porous region, (B) WC inclusion and (C) and (D) Optical image of a machining damage. (C) show the fracture surface with the origin at the surface surrounded by the fracture mirror. Note how the edge is jagged. (D) is a view of the external surface showing many deep longitudinal machining grooves that match with the jagged edge shown in (C).

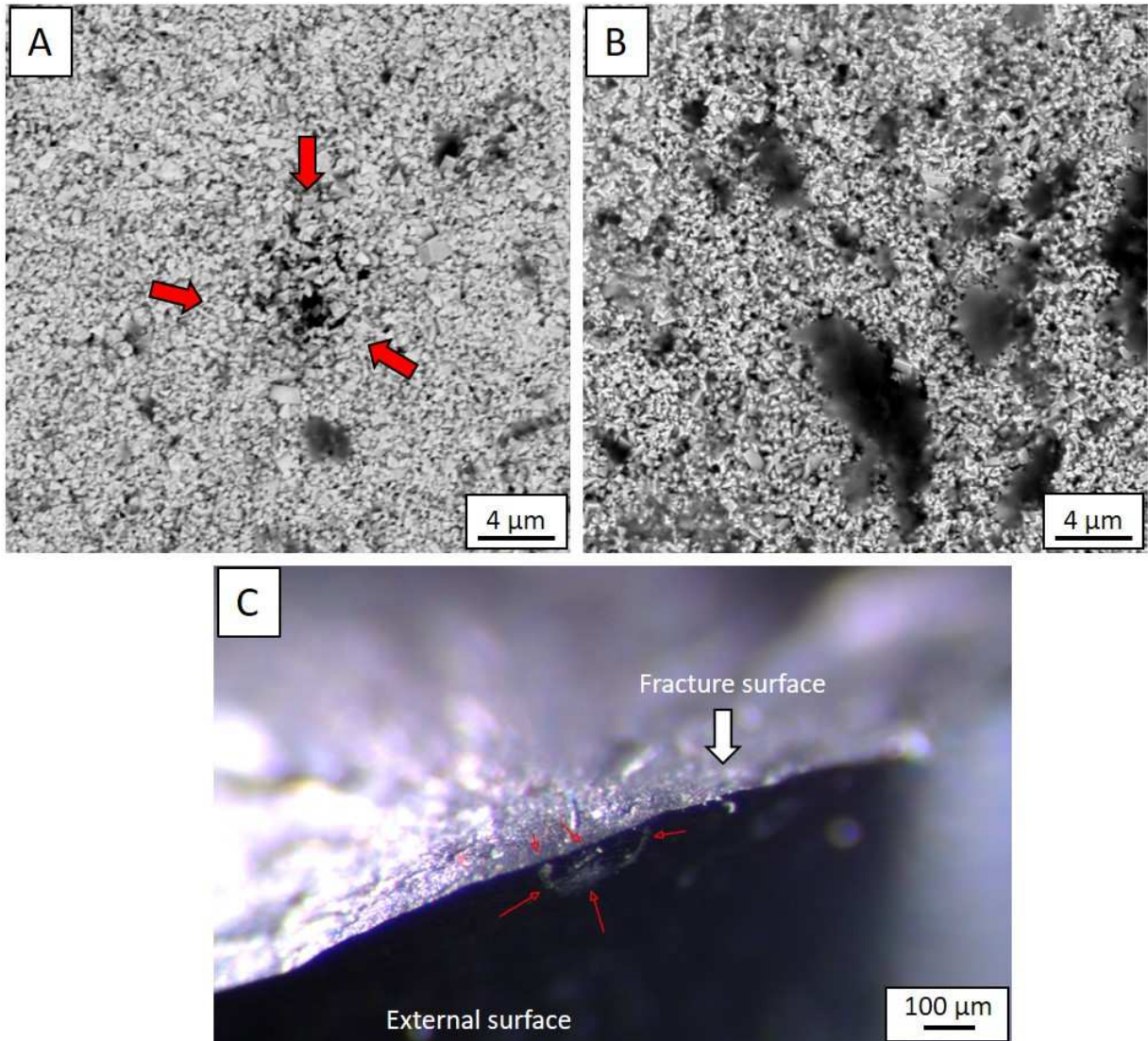


Figure 8. Representative SEM images of the fracture origins in the TSF44h5 (Ultrafine) flexure specimens: (A) small porous region, (B) larger porous region, the submicron black spots are pores while the larger black features are contamination and (C) optical image of machining damage on the external surface of a specimen that was the fracture origin.

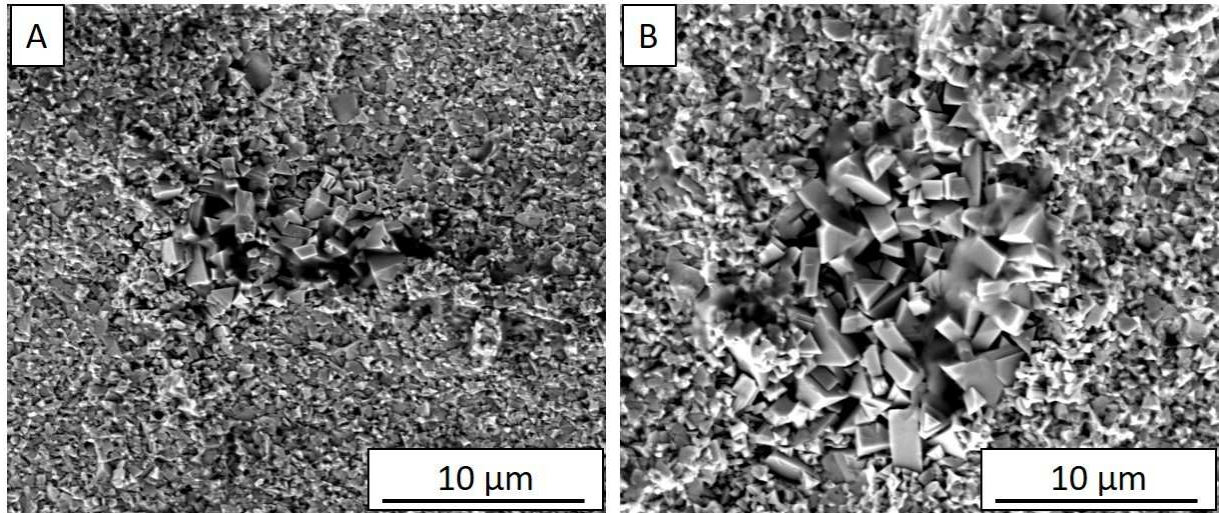


Figure 9. SEM images of the strength-limiting flaws associated with the TSF44h5 (Ultrafine) uniaxial tensile specimens: (A) Porous seam with a cluster of large grains and (B) a porous region with a large grain cluster.

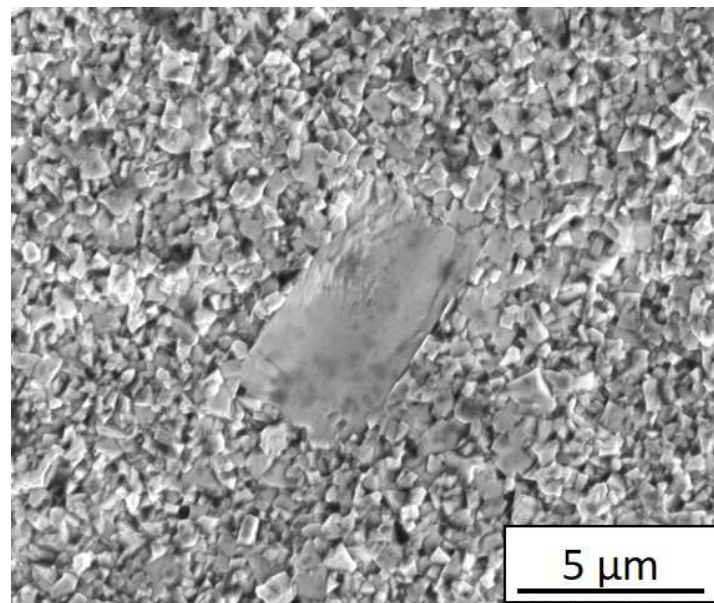


Figure 10. SEM images of the WC inclusion as the fracture origin in the S105 flexure specimens.

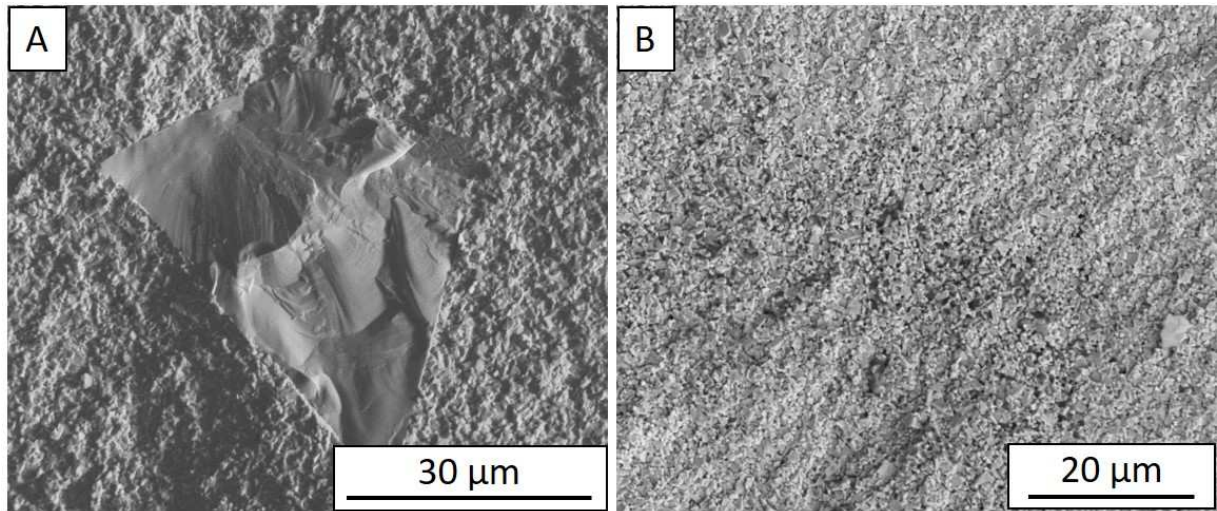


Figure 11. Representative SEM images of the fracture origins identified for the S105 uniaxial tensile specimens: (A) WC inclusion and (B) porous region, all of the black areas are submicron pores.

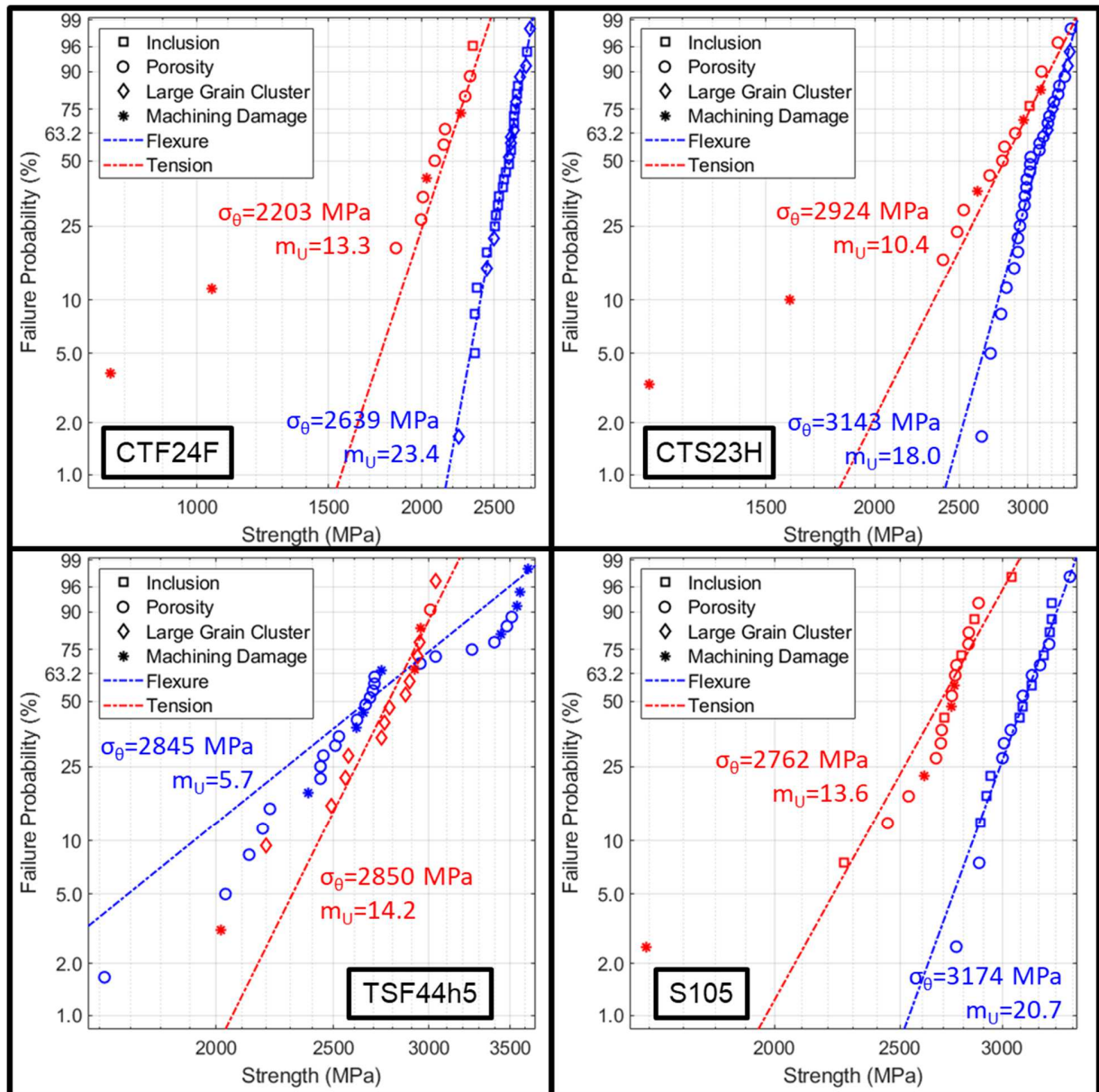


Figure 12. Plots of the results of Weibull analysis for the four materials considering the loading configuration and fractographically-identified strength-limiting flaw analysis: (A) CTF24F (Fine), (B) CTS23H (Submicron), (C) TSF44h5 (Ultrafine), and (D) S105. Specimen data points from flexure are in blue, while tensile specimens are in red. The corresponding dash-dot fit line is plotted based upon the unbiased Weibull modulus (m_U) provided in each plot along with the characteristic strength (σ_θ) for each loading configuration. Note that the specimens that failed due to machining damage have been censored from the numerical analysis but are included in the plot for completeness.

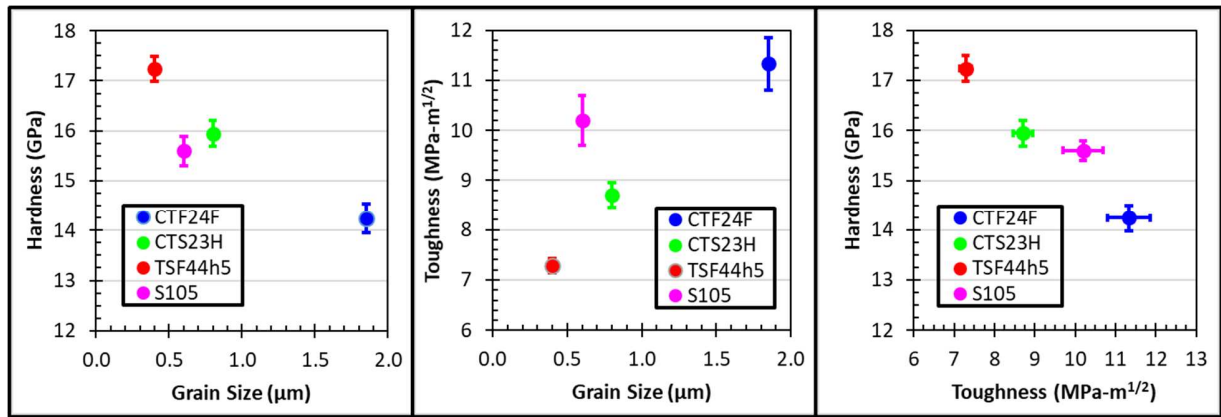


Figure 13. Plots of: (left) hardness versus grain size, (middle) toughness versus grain size, and (right) hardness versus toughness for the four materials.